A&A, 711, A264 (2026)
https://doi.org/10.1051/0004-6361/202555565

Astronomy & Astrophysics

LZ-STAR Survey: Low-metallicity star formation survey of Sh2-284

II. The initial mass function

M. Andersen[1,⋆], A. Brizawasi[2,3], Y. Cheng[4], R. Fedriani[5], J. J. Armstrong[3], M. Robberto[6], M. Aghakhanloo[7], and J. C. Tan[3,7]

[1] European Southern Observatory, Karl-Schwarzschild-Strasse 2, 85748 Garching bei München, Germany
[2] Indian Institute of Science Education and Research (IISER), Mohali, India
[3] Department of Space, Earth & Environment, Chalmers University of Technology, 45293 Gothenburg, Sweden
[4] National Astronomical Observatory of Japan, 2-21-1 Osawa, Mitaka, Tokyo 181-8588, Japan
[5] Instituto de Astrofísica de Andalucía, CSIC, Glorieta de la Astronomía s/n, 18008 Granada, Spain
[6] Space Telescope Science Institute, Baltimore, MD, USA
[7] Department of Astronomy, Univ. of Virginia, Charlottesville, VA 22904, USA

Received 18 May 2025 / Accepted 19 May 2026

ABSTRACT

Context. To fully understand the star formation process, we are compelled to study it in a variety of environments. Of particular interest are how star formation and the resulting initial mass function (IMF) vary as a function of metallicity.
Aims. Using JWST/NIRCam, we observed an embedded young cluster in the vicinity of Sh2-284 (hereafter S284), the HII region associated with the open cluster Dolidze 25, with the aim of studying star formation in a metal-poor (i.e., about 1/3 of solar) environment. In particular, we aim to measure the peak of the IMF.
Methods. Using JWST/NIRCam photometry, we identified the embedded cluster S284-EC1 and resolved its low-mass content. Via a comparison with pre-main-sequence evolutionary tracks, we determined the mass and extinction for the individual cluster members. Extinction-limited samples were created based on the distribution of extinction and the completeness of the data. For the region with a completeness of 60% or higher, we fit a log-normal distribution to the IMF.
Results. Adopting an age of 1 Myr for the cluster members, supported by the high extinction and outflow activity in the region, the peak of the IMF is at $m_c = 0.17 \pm 0.02\,M_\odot$. This value lies toward the low-mass end of the range reported for local young clusters in the literature However, the result is sensitive to the age of the cluster. If an older age of 2 Myr is adopted, the peak mass increases to $0.28\,M_\odot$.
Conclusions. We have found evidence of IMF variation as a function of metallicity, i.e., the peak of the IMF shifts to lower masses as one goes from solar to 1/3 solar metallicity. However, we caution that the result is sensitive to the assumed age of the stellar population, i.e., with peak mass rising if an age older than 1 Myr is adopted. This study further motivates the need for expanded samples of low-metallicity regions and their content to enable more comprehensive measures of the IMF in such environments.

Key words. brown dwarfs – stars: low-mass – stars: luminosity function, mass function – stars: pre-main sequence

1. Introduction

One of the fundamental outcomes of the star formation process is the distribution of masses of stars and brown dwarfs, i.e., the initial mass function (IMF). A key question is whether star formation, including the resulting IMF, depends on global environmental parameters, such as metallicity, density, and magnetic field strength. Substantial work has been carried out to obtain measures of the IMF of the local Galactic field population and in relatively nearby star-forming regions. The main conclusions are that there is little evidence of variations in the observed stellar and brown dwarf IMF down to about $0.03\,M_\odot$ ($30\,M_{\rm Jup}$) (Andersen et al. 2008; Hennebelle & Grudić 2024; Kroupa et al. 2026). For a log-normal representation, the field and nearby star-forming regions are consistent with an IMF with a peak at $0.25\,M_\odot$ (Chabrier 2005).

Some star-forming theories predict variations in the IMF as a function of the environment. In particular, the effect of metallicity has been discussed in the literature, but with a variety of different conclusions. Using hydrodynamic simulations of star-forming clouds with metallicities from $Z = 10^{-1}$ to $10^{-4}\,Z_\odot$, Chon et al. (2021) found the peak of the IMF declines with decreasing metallicity. Their case with $Z = 10^{-1}\,Z_\odot$ yielded a median mass, i.e., close to the peak value, of $0.14\,M_\odot$. However, these simulations did not include any effects of magnetic fields or stellar feedback. On the other hand, Guszejnov et al. (2022) found the opposite effect. In contrast, Myers et al. (2011) and Bate (2014) found little variation as a function of metallicity. Thus, on the theoretical side, the answer is unclear, likely because of the incomplete treatment of the full physics of star formation and feedback.

In any case, different theoretical predictions need to be tested with observations of the IMF, especially targeting the value of its peak mass. However, nearby regions only cover a small range in

⋆ Corresponding author: morten.andersen@eso.org

metallicity, i.e., with values comparable to solar. Thus it is not practical to use these regions to examine dependence of the IMF on metallicity. Studies of massive, more distant Galactic clusters have suggested that the IMF is consistent with the local field IMF down to 0.2 $M_\odot$ (Andersen et al. 2017), but these systems also have a near-solar metallicity. Similar studies in the Large Magellanic Cloud (LMC), where the metallicity is about half solar, have probed the IMF down to about 1 $M_\odot$ (Andersen et al. 2009), also finding general consistency with the local field IMF. A similar conclusion was reached for the lower-metallicity cluster NGC 602 in the Small Magellanic Cloud (SMC) (Schmalzl et al. 2008). Similarly, the field IMF in the SMC has been determined down to 0.37 $M_\odot$ without any evidence of an IMF varying with metallicity (Kalirai et al. 2013). Even lower metallicities ([Fe/H] = −2.6) have been probed in the Coma Berenices dwarf galaxy, where the IMF could be traced down to 0.23 $M_\odot$ (Gennaro et al. 2018), with the conclusion that the derived IMF was also consistent with that of the Galactic field.

Common for the low-metallicity studies quoted above is the fact that they barely reach the Galactic field IMF peak mass of 0.25 $M_\odot$ (Chabrier 2005). Although nearby galaxies are prime targets for studies of the IMF in metal-poor conditions, such studies are restricted by their large distances of 50–60 kpc for the Magellanic Clouds and 43 kpc for Coma Berenices. This problem can be overcome by studying the low-mass IMF in metal-poor environments in the outer Galaxy, given its global metallicity gradient (Daflon & Cunha 2004). Yasui et al. (2023) studied the IMF in the Galactic star-forming region Sh2-209 region, which has an oxygen abundance of −0.5 dex compared to solar. They derived a relatively shallow, i.e., top-heavy, high-end power law index of $\Gamma = -1.0$ (cf., the Salpeter IMF value of −1.35), but with a break mass of 0.1 $M_\odot$ that is smaller than derived from equivalent fitting in the solar neighborhood, i.e., ~0.3 $M_\odot$. Zinnkann et al. (2024) expanded on these results to reach similar conclusion that a denser cluster at low metallicity leads to a top-heavy IMF.

Although recent James Webb space telescope (JWST) observations have enabled the detection of objects down to below a Jupiter mass in nearby star-forming regions (e.g., de Furio et al. 2025), and the identification of pre-main-sequence stars in the distant local group galaxy Wolf–Lundmark–Melotte (Kalari et al. 2025) and objects down to or even below the brown dwarf limit in the Magellanic Clouds (Zeidler et al. 2024), the lowest masses are still most easily reached in the few low-metallicity Galactic young star clusters that are known. The first steps in this direction using JWST were by Yasui et al. (2024) of the Digel 2 cloud where a peak mass of the IMF of ~0.03 $M_\odot$ (with about a factor of 3 uncertainty) was found, substantially below the field IMF peak value of 0.25 $M_\odot$. However, the relatively large uncertainty associated with this measurement indicates that a wider variety of young clusters need to be studied to more securely probe the low-mass IMF in these low-metallicity environments.

The Sh2-284 (hereafter S284) HII region, associated with the Dolidze 25 cluster, is a prime test bed for determining the low-mass IMF in a metal-poor environment. It is located in the Galactic anticenter directions at (l, b)=(211°.9, −01°.3), and has been found to have a ~1/3–1/2 solar metallicity (Negueruela et al. 2015). The distance to the cluster has been under debate, and suggested to be at 5.5 kpc (Lennon et al. 1990) to 6 kpc (Russeil et al. 2007). However, later determinations using more recent low-metallicity stellar evolutionary models have suggested a distance of 4 kpc (Cusano et al. 2011) and 4.5 ± 0.3 kpc (Negueruela et al. 2015). Negueruela et al. (2015) noted that 4.5 kpc is in agreement with a maser 2 degrees away that has a similar radial velocity as the stars in Dolize 25 and thus likely at the same distance. Guarcello et al. (2021) used *Gaia* early data release 3 to determine a distance of 4.5±0.5 kpc for the spectroscopically verified members of Dolidze 25 in Negueruela et al. (2015) that were not identified as binaries. We have repeated the analysis with the current *Gaia 3* catalog (Gaia Collaboration 2023), taking into account the individual parallax zero-points not available in the previous study. Using Gaia stars that are confirmed members of Dolidze 25 by spectroscopy and not a spectroscopic binary in Negueruela et al. (2015), with a RUWE parameter value <1.4 (five stars[1]), we determined a distance of 4.2 ± 0.7 kpc after correcting for the zero-point as prescribed in Lindegren et al. (2021) and adopting 1 over the parallax as the distance. This is consistent with the previous *Gaia* estimate and also with the maser 2 degrees away. Ashraf et al. (2026) analyzed **Gaia** DR3 data for a 3′ radius of the center of Dolidze 25 using DBSCAN to select members and determined a distance of 4.2 ± 0.3 kpc, consistent with the value from spectroscopically selected members. Given these results, we adopted the same distance of 4.5 kpc as in Negueruela et al. (2015) as a fiducial value, but explored the consequences of varying the distance by ±0.3 kpc.

The age of the Dolidze 25 cluster has been estimated in multiple studies. With the distance of 4.5 kpc, Negueruela et al. (2015) estimated the age to be no more than 3 Myr based on the position in the color–magnitude diagram (CMD) of the earliest-type cluster stars. Guarcello et al. (2021) utilized an X-ray selected sample, using the 17′ square field of view of Chandra ACIS-I, to determine the peak of the age distribution to be at 1 Myr, and the median at 1.2 Myr. Kalari & Vink (2015) suggested a median age of 3.5 Myr based on optical spectroscopy of intermediate-mass stars around the center of the cluster. In contrast, Ashraf et al. (2026) used MUSE spectroscopy of the central 1′×2′ (1.3 pc×2.6 pc) of Dolidze 25 to derive an age distribution peaked at 1.53 Myr. The lower age compared to, for example, Kalari & Vink (2015), was suggested to be based on a more comprehensive simultaneous fitting. They used simultaneous fitting of spectral type, accretion, and veiling using low-metallicity atmospheric models. Patra et al. (2024) used broadband near-infrared imaging to investigate three regions of 1–2′ radius within the cluster (marked in Fig. 2). Their results were similar to those of Guarcello et al. (2021); Ashraf et al. (2026) with ages of 1.3–2 Myr for the subclusters and a similar relatively modest extinction toward the sources of $A_V \sim 3$.

Dolidze 25 is surrounded by its HII region with an inner radius of 15′, corresponding to 20 pc. Outside this radius, the HII region interacts with the surrounding molecular material evident at mid-infrared wavelengths due to the emission from the associated dust (Fig. 1). A large scale mid-infrared survey of S284 was performed by Puga et al. (2009) using Spitzer IRAC imaging. Dolidze 25 is surrounded by molecular material where high concentrations of Class I sources were detected. The age of Class I sources is in the range of 0.1–1 Myr, suggesting some age progression across the region, with the younger sources associated with higher-extinction regions at the edge of the HII region.

Puga et al. (2009) identified their region RE 20 pc to the east of the center of Dolidze 25 as a region rich in young sources. Subsequent far-infrared Herschel showed strong emission within region Re (Cheng et al. 2025) with a total gas mass of 760 $M_\odot$.

[1] The *Gaia* IDs are: 3113525799800744320, 3125505670478616192, 3125505704838338816, 3125506014076025088, and 3125506151511957120.

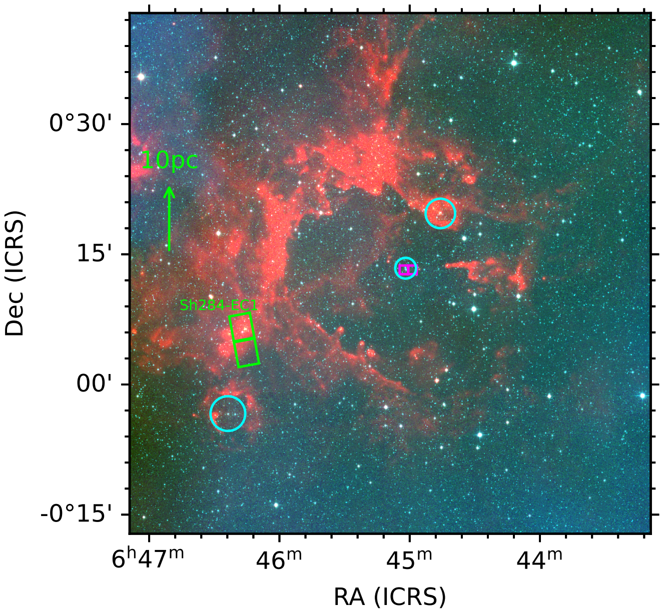

Fig. 1. One degree square field of view WISE 3.6 μm (red), 2MASS Ks, and H (green and blue) image composite of S284, centered on Dolidze 25 and with the target of this study, sh284-EC1 to the east-southeast. A 10 pc scale bar is shown for a distance of 4.5kpc. sh284-EC1 is located 20pc to the east–southeast and the JWST/NIRCam pointing is overlaid as the green boxes with the A module to the north. The fields in Ashraf et al. (2026) and Patra et al. (2024) are shown as the magenta rectangle and the cyan circles, respectively.

The over-density with a full width at half maximum of 0.65 px is hosting a class I star driving a molecular outflow discussed in Cheng et al. (2025).

The current study focuses on the low-mass stellar and brown dwarf content of this embedded region, which we name sh284-EC1. Due to its compactness, youth, and low metallicity, region RE is ideal to probe the early stages of star formation in a low-metallicity environment.

As part of the Low-Metallicity Star Formation Survey in Sh2-284 (LZ-STAR), we present photometry using JWST/NIRCam observations of an embedded region in the shell of S284 within the RE region from Puga et al. (2009), which we term S284 embedded cluster 1 (S284-EC1). Our goal is to assess the distribution of young objects and determine the IMF well into the substellar regime. An overview of the region was presented by Cheng et al. (2025) (LZ-STAR Paper I), including a census of the dense ALMA-detected gas cores and characterization of a potential massive protostar that appears to be forming near the center of the protocluster.

Our paper is structured as follows. In Section 2.1 we discuss the data, their reduction, and the photometry. Section 3 presents the results from the photometry, i.e., the luminosity functions, the CMDs, and the morphology of the cluster. Section 4 discusses the construction of the isochrones, the mass estimates for individual objects, and the derived IMFs under different assumptions about metallicity and age. Finally, we conclude in Section 5.

2. Observations and data reduction

2.1. JWST data

JWST/NIRCam observations were obtained on 19 October, 2022 of S284 through the *F162M*, *F182M*, *F200W*, *F356W*, *F405N*, and *F470N* bands in program ID 2317 (PI: Y. Cheng). The observed $2' \times 4'$ field is shown in Fig. 1. It overlaps with the region 21 within the RE area in Puga et al. (2009) and was chosen due to the embedded sources identified in the Spitzer survey. The three short-wavelength filters of the observations were used to measure the stellar atmospheres of the individual sources. Although a wider wavelength coverage would provide better estimates of extinction, it would create larger differences in the point spread functions (PSFs), sensitivity, and crowding characteristics.

A total of six dithers and six groups resulted in a total integration time of 1739.357 seconds for the shallow2, and 644.206 seconds for the bright2 observations. The readout mode was shallow2 for *F162M*, *F182M*, *F405N*, *F470N* and bright2 for *F200W* and *F356W*. The dither type was fullbox and the pattern tight3, resulting in a relatively homogeneous depth in the mosaic at the cost of a few small gaps in the final mosaics.

The data were reduced using the JWST Calibration Pipeline Version=1.12.5. A few changes were employed to the default parameters. Through the stage 1 processing, we allowed the use of the first read sampling up the ramp to increase the dynamic range of the data, limiting the number of saturated sources. Further, the frames were drizzled together using a final pixel scale of 0.03″, using the relative offsets determined by tweakreg. The data were combined independently for the A and B modules due to a small offset between the two in the mosaicing process.

Figure 2 shows the three-color image of module A, using the three short-wavelength bands. A relatively rich cluster is seen centered at (RA,Dec) = (6:46:15.8501,+0:06:26.197). The green circle with a radius of 1000 pixels (0.65 pc for a distance of 4.5 kpc) illustrates the radius where the cluster population surface number density is similar to the field (see Section 3).

2.2. Photometry

Source detection within the cluster is complicated by both the strong nebulosity and the large dynamic range in the observations. Spurious detections are an issue because of the almost diffraction-limited PSF that introduces artifacts from bright sources that can be identified as point sources. To identify and remove spurious detections, we used an approach similar to that of Andersen et al. (2017), whereby the multicolor data and the dependence on wavelength were utilized. Briefly, a spatially constant PSF was created from the A module using twenty bright, unsaturated isolated stars across the field and a radius of the PSF of 11 pixels adopting the `iraf` implementation of `daophot` (Stetson 1987). The brightest point source objects were identified in the *F200W* image and removed using `allstar`. A fitting radius of 3 pixels was used for all three bands. In the residual image the second brightest stars, at half the threshold as the previous step, were detected and added to the list of the brightest stars. This list was then used to remove stars from the original frame. This process was repeated with subsequently lower thresholds down to four times the background noise. The positions for all objects were then injected into `phot` and `allstar` again in the *F200W* frame and PSF photometry on all sources was performed in one step. The final source list for the *F200W* was then used as an input for the *F162M* and *F182M* filters, where PSF photometry was performed in a similar manner as for the *F200W* band. The centering in each filter was then compared and a source was considered a real source (and not, e.g., a diffraction spot) if the spatial position agreed to within 0.5 pixels between the three bands. The list of vetted sources was then

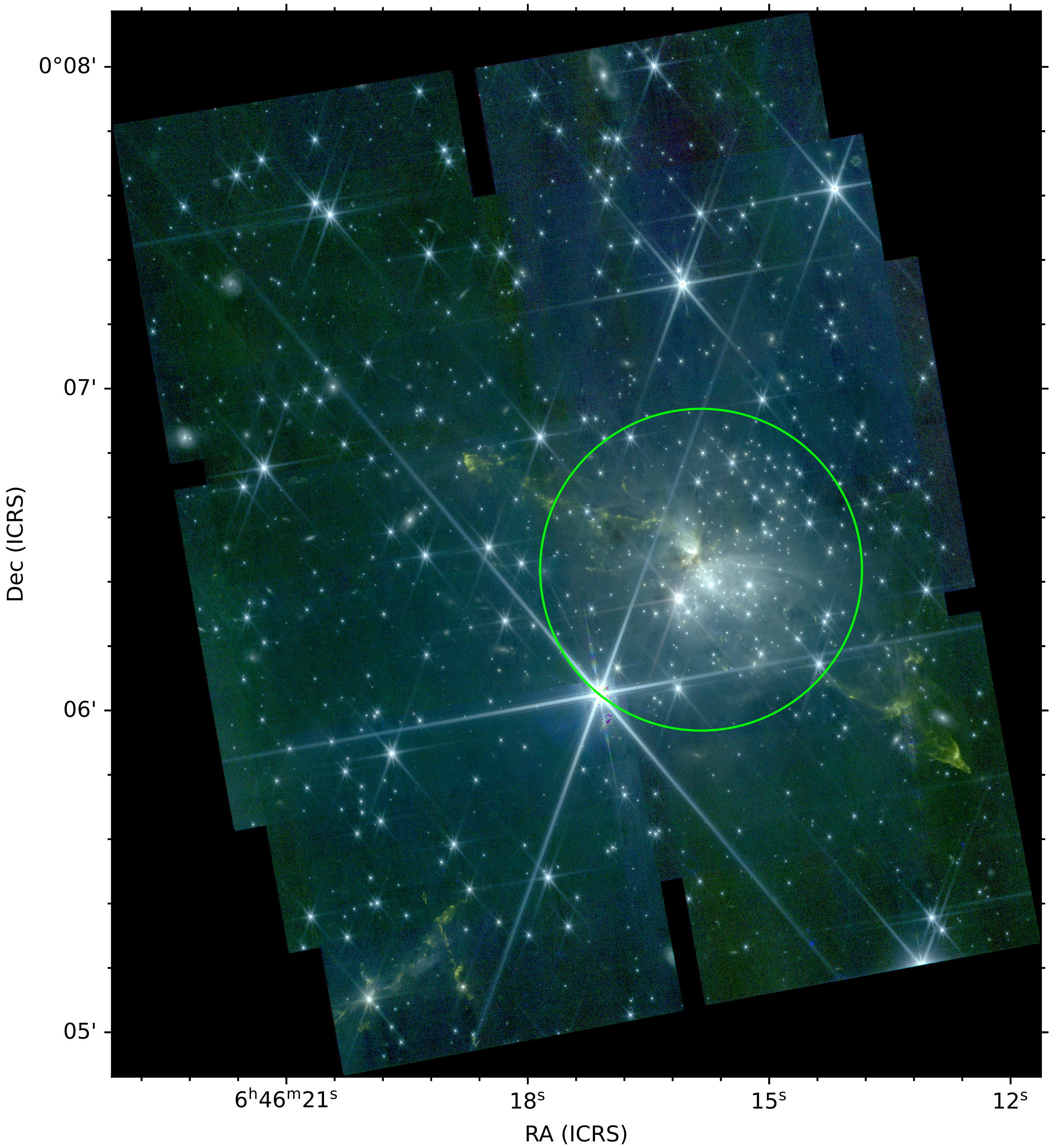

Fig. 2. Color–composite of the short-wavelength NIRCam A-module. Red is *F200W*, green *F182M*, and blue is *F162M*, respectively. The circle indicates a 1000 pixel radius (0.5′, 0.65 pc), with the radius determined in Section 3.3. The scale for all three color channels is logarithmic to emphasize both the bright and faint features.

used for a final process through `phot` and `allstar` in each filter, ensuring that only detections in all three filters were included.

The photometry in each band was zero-point-calibrated using the source list from the pipeline for the sources. Instead of converting the JWST photometry into a more standard system, such as the 2MASS system, we used the models and isochrones converted into the JWST system (see below).

The magnitude errors as a function of magnitude for each filter in the A module are shown in Fig. 3. The sources within the central 1000 pixels of the cluster center, defined below, are marked with thick symbols. The magnitude error generally increases at fainter magnitudes, as expected, but an increase is also seen at bright magnitudes for all three filters. This is due to the usage of the first readout where the zero point for the detector is poorly determined, and thus for bright stars the PSF will deviate in the core from the model PSF. The mass limits for the extinction-limited samples do not include these objects.

For all magnitudes there is a presence of relatively high photometric error points, above 0.1 mag. Upon visual inspection it is clear that these are due to detections of slightly extended objects, typically galaxies and nebulosity structures, which were then excluded due to the photometric error cuts. These objects further had poor reduced chi square fits, due to their extended

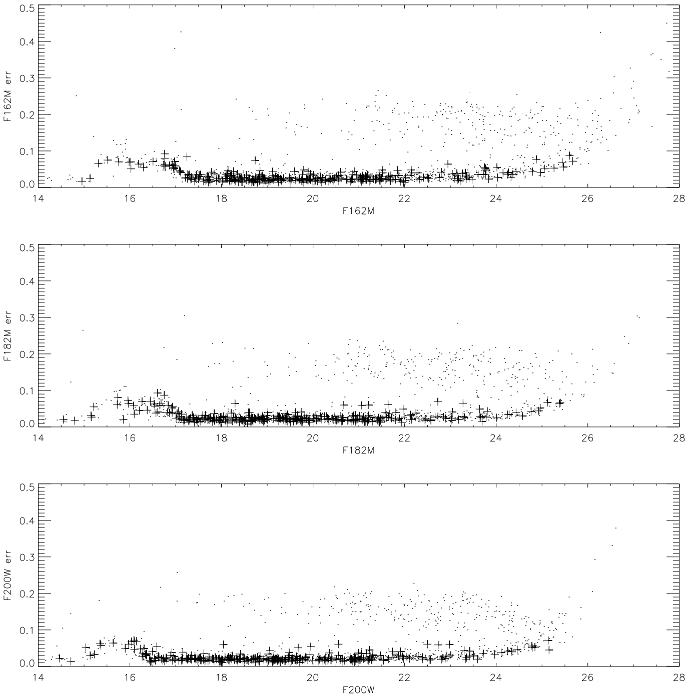

Fig. 3. Photometric errors as a function of magnitude for the stars detected in all the *F162M*, *F182M*, and *F200W* bands in the A module. The thicker cross symbols are for the objects within the designated cluster radius of 1000 pixels.

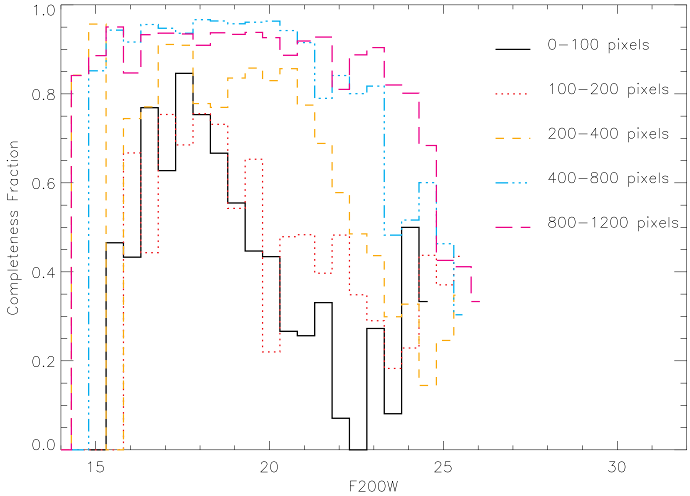

Fig. 4. Fraction of recovered stars from the artificial star experiments. The completeness is shown as a function of radius from the cluster center, illustrating the effects of crowding and nebulosity.

Table 1. Sixty percent completeness limit for the observations as a function of radius from the cluster center.

Annulus pixels	60% mag F200W	60% Mass ($M_\odot$) 1 Myr	60% Mass ($M_\odot$) 2 Myr
0–100	18.88	0.20	0.40
100–200	18.76	0.30	0.40
200–400	22.15	0.03	0.04
400–800	23.39	0.01	0.02
800–1200	24.75	0.01	0.01

Notes. The corresponding 60% limiting mass assuming a 1 Myr and 2 Myr solar metallicity isochrone, a distance of 4.5 kpc, and adopting an extinction of $A_V = 15$.

nature. The total number of objects detected with photometric errors smaller than 0.1 mag in all three bands is 1092 for the A module and 874 for the B module, respectively.

2.3. Completeness corrections

Estimating the sensitivity of the observations is complicated due to the relatively high source density and nebulosity within the cluster region, and these factors are potential sources of biases in the source catalog. Artificial star experiments have been carried out to quantify how source counts might have been affected as a function of magnitude and as a function of position in the field of view. Following the approach in (e.g., Andersen et al. 2009; Gennaro et al. 2011; Andersen et al. 2017), we have inserted point sources with colors and magnitudes similar to the observed objects. To avoid affecting the characteristics of the observations, 25% of the detected sources have been inserted, i.e., 300–350 sources per run. This is a slightly higher fraction than in, for example, Andersen et al. (2017), which is allowed by the level of crowding being relatively low in S284-EC1. Indeed, the main effects for this cluster are the nebulosity and diffraction spikes from the bright stars. Further, the relative surface density profile of the inserted sources is similar to that of the observed objects. This was in practice done by, for each object selected as an artificial star from the source list, calculating the distance from the assigned cluster center and then placing the artificial source at the same distance, but at a random angle. A total of 2000 runs with different random star populations were performed. The data analysis was identical as for the science data and an artificial star was considered retrieved if the recovered source was within 0.5 pixels of the true position.

Fig. 4 shows the completeness as a function of magnitude, both within the cluster and in the general field. Away from the cluster center (which is defined in Section 3), the recovery fraction is close to 100% across most of the magnitude range, with a slow decline for F200W > 22 mag. Closer to the cluster center, the presence of nebulosity affects the completeness in several ways. The nebulosity results in a higher background, and hence background noise, and the fainter sources are more easily lost. The density of stars is also higher, resulting in predominantly fainter sources being lost. The high background also means a lower completeness for brighter sources, since the saturation limit is more easily reached. In the center of the cluster (0.065 pc radius), the completeness is, in general, low across all magnitudes, but in particular for faint magnitudes, as expected. The completeness falls below 60% at around F200W = 19.0, corresponding to a 0.2 $M_\odot$ half-solar metallicity, 1 Myr old star seen through an extinction of $A_V = 10$ (Baraffe et al. 2015; Allard 2014). Outside a radius of 200 pixels (6″), the 60% completeness is above F200W = 22, well into the brown dwarf regime.

The completeness correction for each individual object was determined by using the completeness determined for the artificial stars in the same radial bin as the observed object. A Fermi function was fit to the completeness curves (Gennaro et al. 2011; Andersen et al. 2017), and the corresponding completeness for the object was determined from that fit.

The photometric depth of the annuli were determined as the magnitude where the 60% completeness limit is reached (as in, e.g., Gennaro et al. 2011; Andersen et al. 2017). Table 1 summarizes the limits as a function of radius from the center of

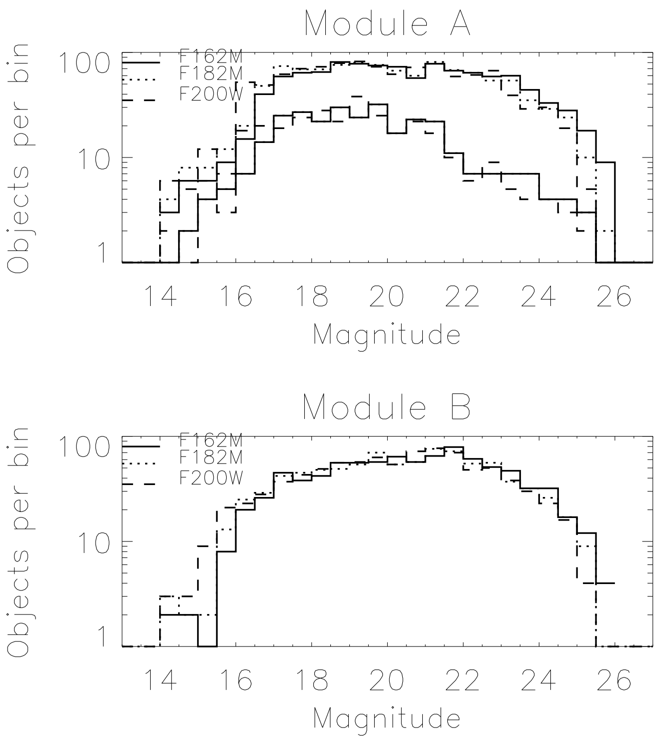

Fig. 5. Observed luminosity functions for the *F162M*, *F182M*, and *F200W* bands for all objects in both modules. The lower histograms in the A module are for the central 1000 pixels around EC1.

the cluster. As expected, because of the nebulosity and surface density of the cluster members, the completeness is a strong function of radius. We note that outside 200 pixels, which corresponds to 0.13 pc for a distance of 4.5 kpc, the observations are sensitive and over 60% complete for a 30 $M_{\rm Jup}$ for a 1 Myr isochrone and 40 $M_{\rm Jup}$ for a 2 Myr isochrone seen through an extinction of A_V = 15 mag beyond 200 pixels from the cluster center. At higher masses, less extinction, or larger radii, the completeness is higher. We adopted the 60% completeness limit in the subsequent analysis. The photometry was corrected for the incompleteness on a star-by-star basis in constructing the IMF histograms.

3. Results and analysis

We present direct results from source counts and photometry. The luminosity functions for the filters and both modules are discussed before the CMDs, and the radial profile of the cluster is presented.

3.1. Luminosity functions

Fig. 5 shows the uncorrected luminosity functions for the three filters and for the A and B modules. The shapes of the luminosity functions for the different filters are similar with a slight shift with the filter, as expected for the colors of both pre-main-sequence cluster members and field stars.

The gradual turnover for both the cluster and control fields at faint magnitudes is largely due to the lack of field stars toward the anticenter at faint magnitudes. This is in agreement with Galactic models (e.g., Robin et al. 2012). Galaxies do contaminate the observations, but due to the depth of the observations there are relatively few galaxies and for the magnitude range of these observations the small faint galaxies are not detected (Rieke et al. 2023).

3.2. Color–magnitude diagrams

Fig. 6 shows the *F162M-F182M* versus *F162M* and *F162M-F200W* versus *F200W* CMDs for both modules. Overplotted are 1 Myr solar metallicity and half solar metallicity isochrones and an extinction vector corresponding to A_V = 15. Masses are marked on the 1 Myr solar metallicity isochrone. The location of the 1 Myr solar metallicity isochrone reddened by A_V = 15 is also shown. Objects within 1000-pixel radius from the cluster center are marked in red. The CMDs for the control field are much more concentrated than for the cluster field, confirming the presence of extinction across the field of view of the cluster in the A module. This is more pronounced for the central region, i.e., red points, where a reddening of up to A_V = 15 is observed.

The different distributions are also seen in the histogram of the colors between the cluster and control fields in Fig. 7. The reddening of the cluster necessitates extinction-limited samples for an unbiased view of the cluster population across masses. Based on the estimated extinction values for the control field, there is a foreground extinction toward S284-EC1 of A_V = 4, which can both be along the general line of sight and from the larger star-forming region.

The field population, as traced by the B module, is almost exclusively located at blue colors of F162M-F182M~0.3, whereas the A module region peaks at 0.4 mag, extending to higher values. This indicates that an extinction-limited sample excluding the low-extinction objects will be effective in removing most of the field contamination from the cluster field (see below).

3.3. Cluster center and cluster radius

We adopted the massive protostar discussed in Cheng et al. (2025) as the center of the cluster. The size of the cluster was determined as the radius where the surface number density determined from the radial profile is similar to that of the surface number density in the control field. The star counts were corrected for completeness. Due to the completeness limit in the central parts of the cluster, only stars down to *F200W* = 19.55 were used for the profile. Figure 8 shows the surface number density profile for the cluster. The horizontal line shows the surface number density in the control field for the same magnitude limit. The cluster surface number density profile follows a King profile with a core radius of 0.1 pc out to a distance of 1 pc.

We adopted a radius of 1000 pixels, corresponding to 0.65 pc, for the cluster in the following analysis. This corresponds to the point where the cluster surface number density is about 20% of the background population and is a compromise between including more cluster members in the sample and limiting the background contribution. Within the 1000 pixel radius from the cluster center, there is a total of 305 objects.

4. The initial mass function of S284-EC1

Here we discuss the steps involved in the estimation of the IMF. The isochrones were created based on stellar evolutionary models and atmospheres, with an investigation of the effects of different metallicity. The extinction and mass for the individual objects were determined by de-reddening the sources to the isochrones and the adopted mass ranges suitable for determining the IMF, creating extinction-limited samples, and investigating the field star contamination of the cluster field. Power-law and

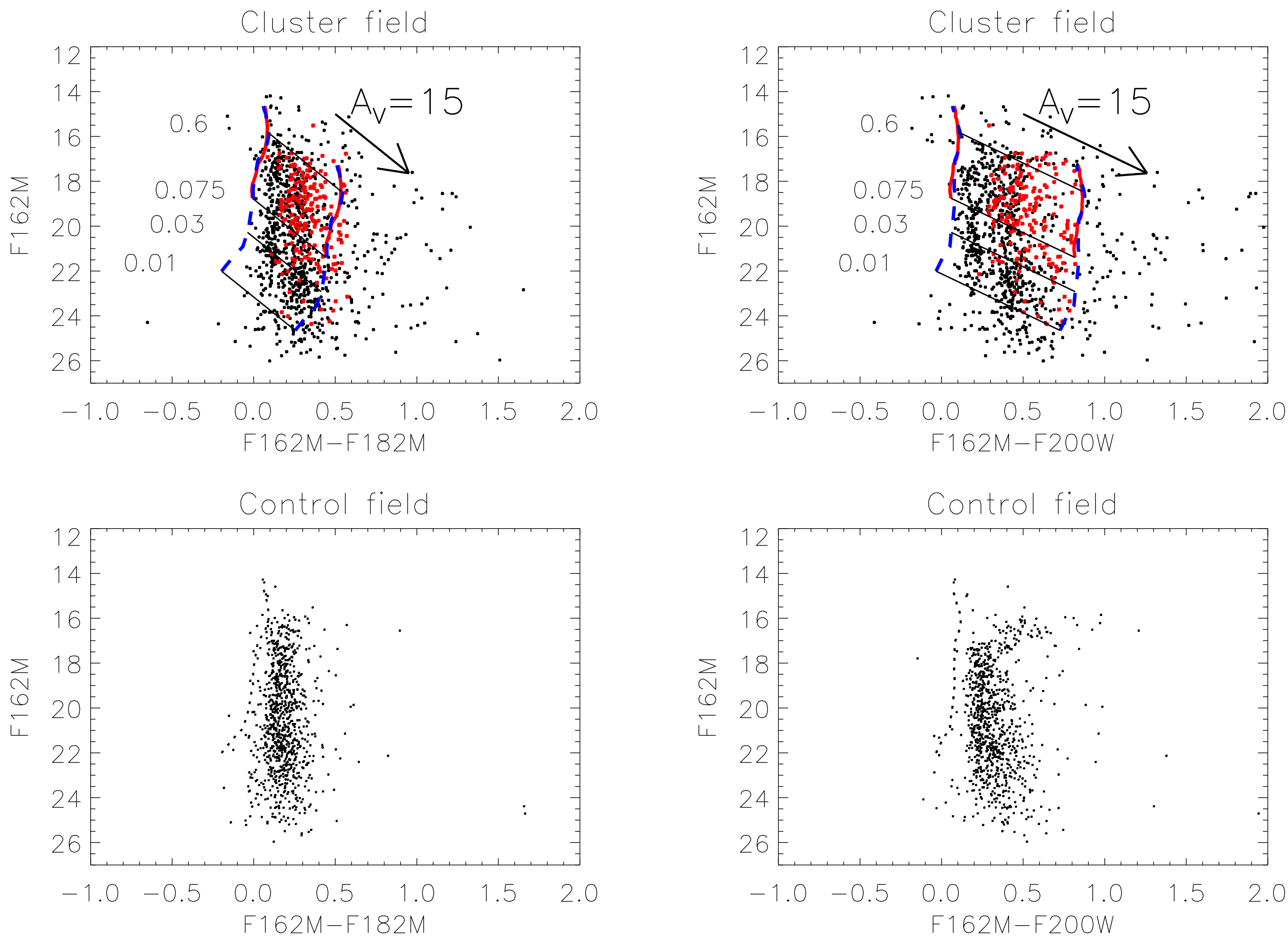

Fig. 6. CMDs for the F162M, F182M, and F200W filters. Overplotted are solar (dotted lines in blue) and half-solar 1 Myr isochrones (solid lines in red) from Baraffe et al. (2015) using the atmospheres from Allard (2014). To illustrate the location of the extinction-limited samples, the isochrones have also been shifted by $A_V = 15$. The locations of 0.6 $M_\odot$ and 0.075 $M_\odot$ stars are shown, the latter being the lowest mass of the half-solar metallicity isochrone. The 0.6 $M_\odot$ for a 1 Myr isochrone is also the brightest object considered in the fits to the IMF. The extinction vector corresponding to $A_V = 15$ is shown in the CMDs for the cluster field. Bottom panels: similar data points as in the upper panels, but for the control region. A 1 Myr solar metallicity isochrone, shifted to the distance of S284, is shown.

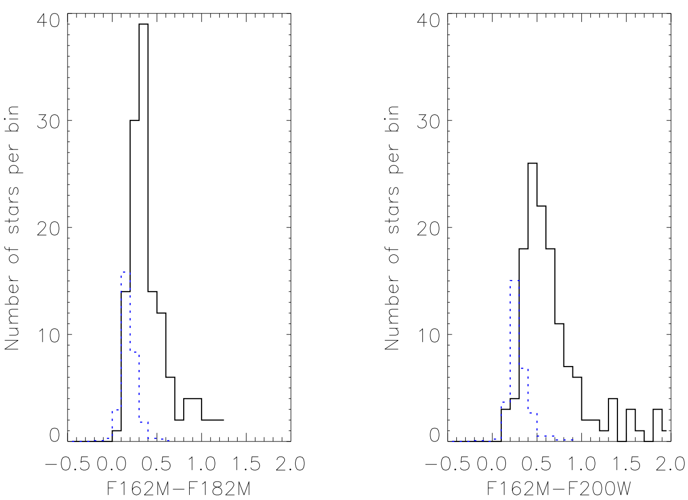

Fig. 7. Distribution of colors for the cluster region and the control field scaled to the same area as the cluster region for both F162M-F182M and F162M-F200W. The control field has been scaled to the same area as the cluster circle.

log-normal fits were made for the sources from the extinction-limited samples and the results were compared with those from nearby star-forming regions and the Galactic field. Potential biases in the derived IMF are discussed.

4.1. Isochrones for low-mass objects

We adopted the interior models from Baraffe et al. (2015) for the appropriate isochrone ages and metallicity. The effective temperature and gravity from the Baraffe et al. (2015) models were then used as inputs for the Allard (2014) atmospheric models. These were then convolved with the appropriate JWST filter profiles to obtain the absolute magnitude in the observed pass bands.

Whereas the Baraffe et al. (2015) models extend from 1.4 $M_\odot$ down to 0.01 $M_\odot$ for solar metallicity, they reach down to the brown dwarf limit for the $[\frac{Z}{Z_\odot}] = -0.5$ calculations (the brown dwarf limit is 0.075 $M_\odot$ for this metallicity). The metallicity of S284 has been measured to be about a third to half solar (Negueruela et al. 2015). The closest in metallicity from Baraffe et al. (2015); Allard et al. (2012) models are thus the −0.5 dex calculations.

Since the subsolar metallicity atmospheric models do not extend below roughly the brown dwarf limit, we were forced to use the solar metallicity models to estimate the properties of the individual brown dwarfs and to estimate the full low-mass IMF in the outer parts of the cluster. This illustrates the need for

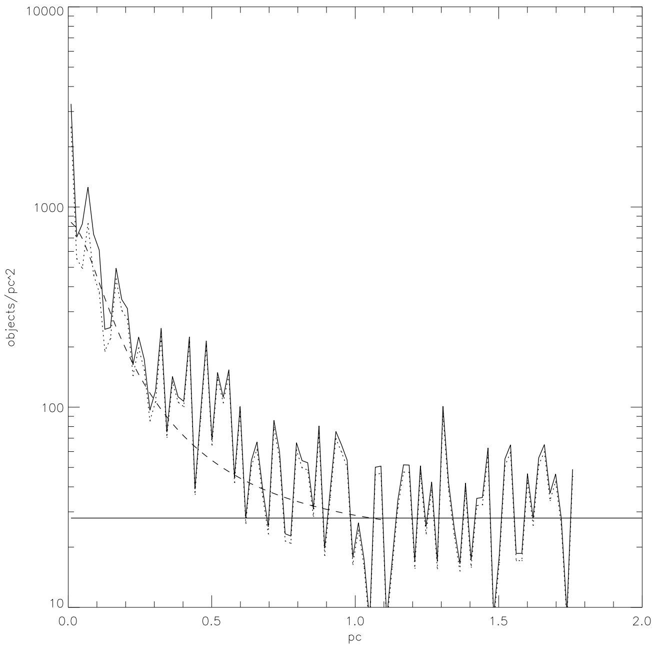

Fig. 8. Radial profile centered on EC1, i.e., (RA,Dec) = (6:46:15.8501,0:06:26.197) for module A. The solid horizontal line indicates the surface number density of stars in the B module, taken as the field population surface number density. Objects brighter than F200W = 19.5 were used, to ensure completeness in the central parts of the cluster as outlined above. The best-fit King profile is shown with a core radius of 0.1 pc.

improved low-metallicity models applicable for low masses and young ages.

The 1 Myr solar and half-solar metallicity isochrones are plotted in Fig. 6. The difference in metallicity shows itself in two different ways: the low-metallicity track is bluer (hotter) and for a given mass the stars are more luminous. This is largely due to the lower opacity at lower metallicity. The combination of the low-metallicity tracks being brighter and blue can to some degree be mimicked as extinction; however, the effect is relatively subtle. The difference in magnitude for a given mass for a 1 Myr and 2 Myr isochrone depends on the mass, but can be 0.1 mag. We have compared the results of fitting down to 0.03 $M_\odot$ using the solar-metallicity isochrones, with the fits only extending to 0.08 $M_\odot$ using the –0.5 dex metallicity isochrones below.

4.2. Field object contamination

An inherent issue in determining the cluster population is distinguishing cluster members and the general field star population. However, given the location of S284 toward the Galactic anticenter from the Sun, the field star contamination is relatively minor compared to other clusters in the Milky Way. In particular, due to the decreasing number density of stars as a function of Galactocentric distance, the majority of field stars within the field of view will be foreground stars.

We utilized the B module as a measure of the field star population toward S284-EC1. Within the B module, we determined a surface number density of 120 stars/arcm^2. The Galactic models by Robin et al. (2012) predict 135 stars/arcm^2, in agreement with what is measured in the B module within 1.5σ. The CMDs for the B module were thus used as the control field, as discussed below.

The sensitivity of JWST means that galaxies are a potential contaminant within our field of view. Indeed, the images do contain several galaxies that are easily identified by eye. Comparing with the JADES results on the surface number density of galaxies (Rieke et al. 2023), the contamination is rather limited for the magnitude range probed in this study. Furthermore, the brighter galaxies tend to be well resolved, and were thus excluded from the photometric catalog based on their full width at half maximum, roundness, and sharpness. Finally, the general line of sight population is expected to be statistically the same for the two modules with different extinction distributions, and thus they were removed as a part of the statistical field star subtraction and the extinction-limited samples.

4.3. Mass range and extinction-limited samples

The mass and extinction were determined for each object by dereddening it in the CMD to the adopted isochrone, following the approach in, for example, Andersen et al. (2017). The extinction law was adopted from Cardelli et al. (1989), convolved with the JWST filter profiles. The mass of each object was thus derived using the F162M-F182M versus F162M and F162M-F200W versus F162M CMDs independently and assuming either a 1 or 2 Myr isochrone.

The mass range fit is affected by the adopted distance to the cluster, the completeness of the observations, the minimum and maximum extinction for the extinction-limited sample, and the stellar evolutionary models adopted. The IMF was fit under different assumptions of the parameters within their expected range. Specifically, the IMF was calculated under the assumption of a distance of 4.2, 4.5, and 4.8 kpc to cover the uncertainty presented in Negueruela et al. (2015), and adopting either a 1 or 2 Myr isochrone. These cover the range of ages suggested in Guarcello et al. (2021). However, this was determined for the cluster as a whole and the age distribution was found to be quite wide. We favor a young age for the S284-EC1 cluster based on several factors: the cluster is deeply embedded, with a typical extinction of 10~ A_V, which is high considering the lower dust-to-gas ratio expected for a metallicity similar to that of the LMC (Koornneef 1982). Furthermore, the region is associated with strong protostellar outflows (Cheng et al. 2025; Jadhav et al. 2025), which suggests youth. Thus we adopted the 1 Myr as our fiducial case, but examined the impact on the IMF results if the older age was used.

Figure 9 shows the extinction distribution for the stellar content within a 1000 pixel radius of the cluster center, assuming the 1 Myr low-metallicity isochrone. The results are similar for the solar-metallicity isochrone and for an age of 2 Myr. The distribution peaks at an extinction of A_V = 8 and extends to larger values. The extinction values for field objects, as determined by projecting the objects to the –0.5 dex metallicity 1 Myr isochrone, are shown as the dotted histogram[2]. Most of the objects have a relatively low extinction of A_V = 4.5. Thus, to limit the field star contamination, we adopted a minimum extinction of A_V = 4.5 for the cluster sample.

Since low-mass objects with high extinction would be lost due to the sensitivity limit of the observations, one can bias the IMF if an extinction-limited sample is not created (e.g., Andersen et al. 2006). For high extinction, we limited the sample to A_V = 15, which, as is noted in Table 1, corresponds to a mass

[2] The true extinction for the field objects should be determined knowing their spectral type and then de-reddening based on this information. However, since the purpose here is to remove the field contribution, de-reddening to the isochrone illustrates their contribution to the cluster field.

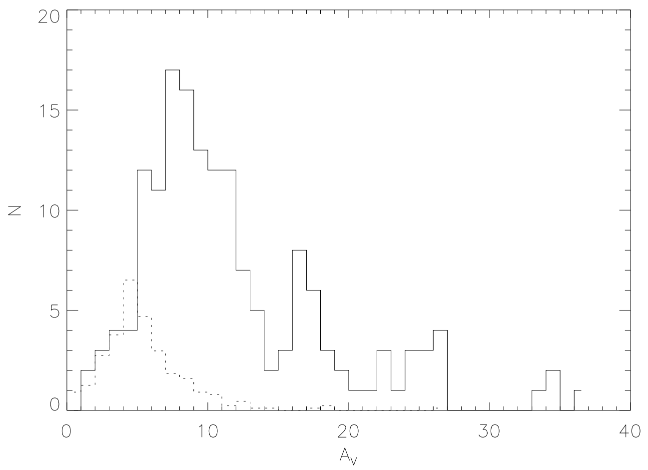

Fig. 9. Distribution of extinction values for the central 1000 pixel radius of the cluster (solid histogram) and for the B module scaled to the same area as the cluster circle. A –0.5 dex, 1 Myr isochrone was assumed and objects in the mass range 0.1–0.7 $M_{\odot}$ were sampled.

limit of 0.03 $M_{\odot}$. A deeper extinction limit would increase the lower mass limit, while at the same time only adding a few more objects at higher masses. The final number of detected sources in the cluster out to a 1000 pixel radius is thus 135 in the mass interval 0.03–0.6 $M_{\odot}$ for a 1 Myr isochrone in the F162M-F182M CMD.

4.4. Initial mass function

Building on the results in Sections 5 and 4.1–4.3, we determined the IMF for the cluster EC1 located east-southeast of Dolidze 25. Adopting a 1 Myr isochrone and a distance of 4.5 kpc, the objects have been de-reddened in the CMDs. An extinction-limited sample was constructed based on Fig. 9 to reduce the foreground contamination. The sample used for the IMF has determined extinction values of between A_V=4.5–15. Based on the completeness corrections summarized in Fig. 4, we determined that at 200 pixels radius (0.13 pc) the data are 60% complete for a 30 Mjup object seen through A_V=15. For larger radii, out to 1000 pixels (0.65pc), the maximum radius we used for the sample, the completeness is higher, resulting in a higher overall completeness. The overall completeness in the lowest-mass bin is 84%, rising to 90% for higher masses. The completeness-corrected and field-star-subtracted IMF was calculated and is presented in Table 2. To test the sensitivity of the results, we further present the results for an adapted age of 2 Myr as well as for varying the distance between 4.2 and 4.8 kpc.

4.4.1. Log-normal fits to the IMF

Based on the assumptions outlined above, we have fit a log-normal function to the IMF for 1 and 2 Myr isochrones to the completeness limit of the data of 60% and for objects below a mass of 0.6 $M_{\odot}$, at which point the objects saturate. The errors are assumed to the square root of the number of objects in each bin. The mass functions are in general well fit by a log-normal distribution. Figure 10 shows the mass functions and best log-normal fits for the extinction-limited sample, adopting a distance of 4.5 kpc, for ages of 1 and 2 Myr, for de-reddening the sources in both combinations of the CMDs, and for the region defined by the annulus from 200–1000 pixels in radius from cluster center. The annulus was chosen due to it being able to probe to a mass limit of 0.03–0.04 $M_{\odot}$, a substantially lower mass limit than in the center of the cluster.

For the fiducial age of 1 Myr, the best-fit log-normal distributions yield a mean peak mass of $m_c = 0.16 \pm 0.02\, M_{\odot}$. The peaks and widths of the log-normal fits are listed in Table 2, both for the mass functions in Fig. 10 and for the cases of different adopted distances and ages of the cluster.

We see that our fiducial value for the peak of the IMF is significantly smaller than the peak of the field IMF of 0.25 $M_{\odot}$ (Chabrier 2005), independent of the filter combination and the distance adopted. Our value is also similar to the low peak masses found in the survey by Damian et al. (2021) of a range of clusters within 2 kpc of the Sun. The dependency on age and distance is as expected: assuming an older or more distant population skews the IMF to higher masses. Table 2 shows the fits based on adopting a shorter and larger distance. The change in the peak mass varies by ±0.02 $M_{\odot}$. A pre-main-sequence object gets fainter with age, and thus a given observed magnitude will be interpreted as a higher-mass object. In particular, we note that if we adopt an age of 2 Myr the peak mass of the IMF rises to a mean value of 0.25 ± 0.03 $M_{\odot}$. The implications of our derived IMF parameters are discussed further in Section 4.5.

We performed the same fits to the stellar content, but now using the models with subsolar metallicities. The cluster center was again avoided due to the completeness limit. The fitting was done in the same manner as for the solar metallicity models, changing age and distance in the same manner. The results are provided in Table 3.

The fits provide results that are broadly consistent with those obtained with the solar metallicity fits. In particular, when adopting a 1 Myr isochrone the peak mass is found to be about 0.16 ± 0.05 $M_{\odot}$, which is significantly below that of the local Galactic field population. However, again, if a 2 Myr isochrone is adopted, this mass scale is raised and would be consistent with that of the local value. We note that the uncertainties in the fit results for the lower-Z models are larger due to the smaller fit range used.

4.4.2. Cluster-wide power-law fits to the stellar content

The log-normal fits were carried out for the regions of the cluster with the highest completeness, i.e., outside a 200 pixel radius. However, despite the poor completeness for both the brightest and faintest stars closer to the center, the IMF here can still be probed over a more limited mass range. Table 4 summarizes the best-fit power-laws for the mass range 0.2–0.7 $M_{\odot}$ for 1 Myr isochrones and 0.3–0.8 $M_{\odot}$ for the 2 Myr isochrones for the whole cluster, i.e., from 0–1000 pixels in radius.

The uncertainties on the individual power-law fits are relatively large due to the small mass range fit, dictated by the completeness limit and the saturation limit. Since the extinction cannot be estimated for the higher-mass stars that are saturated, they are not included in the discussion. The average power law index for the different fits and metallicities is −1.0 ± 0.3, i.e., slightly shallower than, but still consistent with, the Salpeter value, and also consistent with the slightly top-heavy higher-mass IMFs measured in the LMC (Schneider et al. 2018) and in other outer Galaxy star-forming regions (Yasui et al. 2023).

4.5. IMF biases

Several factors can affect the derived IMFs in addition to age and distance. These include circumstellar disks, binarity, choice of extinction law, and the metallicity used to create the evolutionary tracks, which we discuss below.

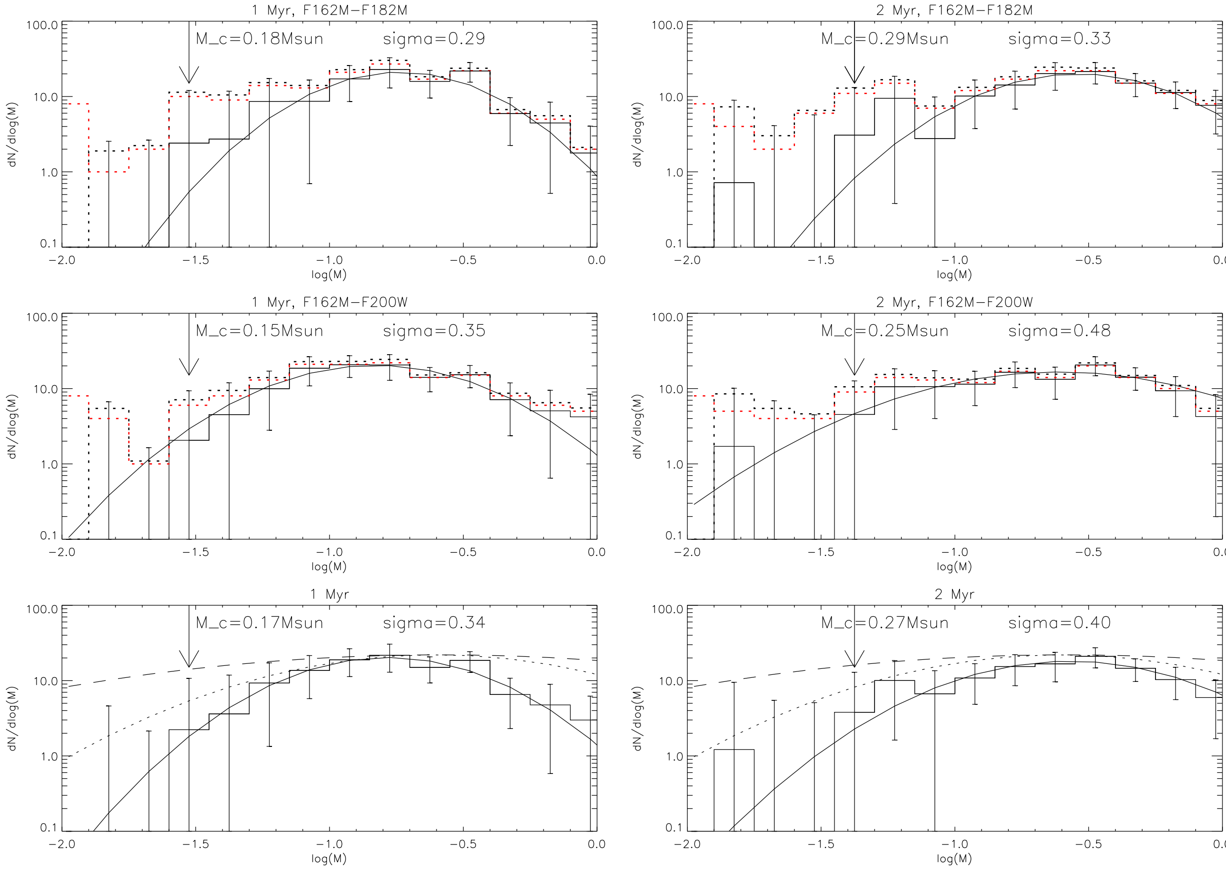

Fig. 10. IMF for the annulus 200–1000 pixels from the cluster center. Both the F162M-F182M vs. F162M and F162M–F200W vs. F200W CMDs were used for the mass estimates of individual sources and ages of 1 and 2 Myr solar metallicity isochrones were adopted. The limit of the fits, i.e., the 60% completeness limit, is shown as an arrow in each diagram and is 0.03 $M_{\odot}$ and 0.04 $M_{\odot}$ for ages of 1 and 2 Myr, respectively. In each plot the dotted histogram shows the completeness-corrected IMF before field subtraction and the solid lined histogram the field-star-corrected IMF. The dotted red lines show the histogram for the cluster field before completeness correction and field subtraction. The two bottom panels are the average of the two filter combinations. Overplotted are the Chabrier (2005) IMF as a dotted line as well as the ONC IMF determined by Gennaro & Robberto (2020) as a dashed line.

Table 2. Parameters for the log-normal distribution fits, with the assumed ages and distances noted adopting the solar metallicity evolutionary models of Baraffe et al. (2015).

Age Myr	Filters	Dist kpc	m_c $M_{\odot}$	σ $M_{\odot}$	Filters	m_c $M_{\odot}$	σ $M_{\odot}$	bin
1	F162M,F182M	4.5	0.18±0.03	0.29±0.08	F162M,F200W	0.15±0.03	0.36±0.1	0.15
2	F162M,F182M	4.5	0.29±0.05	0.33±0.10	F162M,F200W	0.27±0.06	0.40±0.13	0.15
1	F162M,F182M	4.2	0.16±0.03	0.35±0.10	F162M,F200W	0.14±0.02	0.36±0.09	0.15
2	F162M,F182M	4.2	0.22±0.03	0.34±0.08	F162M,F200W	0.22±0.04	0.40±0.11	0.15
1	F162M,F182M	4.8	0.18±0.04	0.38±0.12	F162M,F200W	0.17±0.03	0.35±0.10	0.15
2	F162M,F182M	4.8	0.28±0.04	0.35±0.09	F162M,F200W	0.28±0.04	0.33±0.08	0.15
1	F162M,F182M	4.5	0.16±0.05	0.45±0.19	F162M,F200W	0.15±0.03	0.35±0.10	0.10
2	F162M,F182M	4.5	0.31±0.08	0.36±0.13	F162M,F200W	0.29±0.06	0.36±0.12	0.10

Circumstellar disks are common around young stellar objects (YSOs). The inner part of the disk can be heated to 2000 K and they can in some cases be detected through their infrared emission at and beyond 2 μm, i.e., excess to the stellar photosphere. If not corrected for, this excess emission could bias the determined IMF. Mužić et al. (2019) performed a detailed analysis of the effects of disks on the IMF for the Rosette nebula, which has an intermediate disk fraction. They found the effects on the determined masses were typically minor, and thus the IMF was only marginally affected. Nevertheless, we investigated the effect assuming a circumstellar disk fraction of 40% and a disk excess in the F200W band uniformly chosen between 0 and 0.2 mag. For the 1 Myr isochrone, the change in the peak mass is modest, increasing the peak mass by 0.01 $M_{\odot}$, confirming the results from Mužić et al. (2019) that the impact of circumstellar disks on the IMF is very limited.

There are a variety of extinction laws that may be applicable to dust in the diffuse ISM and denser star-forming clouds. To illustrate the difference for the IMF that is induced using the extinction law of Fitzpatrick (1999) rather than that of Cardelli et al. (1989), we see that the best log-normal fit using the F162M-F182M versus F162M CMD and the 1 Myr isochrone is 0.18 $M_{\odot}$,

Table 3. Parameters for the log-normal distribution fits, with the assumed ages and distances noted adopting the evolutionary models of Baraffe et al. (2015) with a metallicity of −0.5 dex. All bins are 0.1 dex.

Age Myr	Filters	Dist kpc	m_c $M_\odot$	σ $M_\odot$	Filters	m_c $M_\odot$	σ $M_\odot$
1	F162M,F182M	4.5	0.17±0.05	0.40±0.18	F162M,F200W	0.156±0.06	0.43±0.22
2	F162M,F182M	4.5	0.28±0.04	0.29±0.07	F162M,F200W	0.26±0.03	0.27±0.07
1	F162M,F182M	4.2	0.16±0.07	0.44±0.23	F162M,F200W	0.10±0.11	0.55±0.44
2	F162M,F182M	4.2	0.24±0.03	0.30±0.07	F162M,F200W	0.24±0.03	0.31±0.08
1	F162M,F182M	4.8	0.21±0.04	0.29±0.09	F162M,F200W	0.12±0.20	0.74±1.11
2	F162M,F182M	4.8	0.28±0.05	0.32±0.10	F162M,F200W	0.26±0.04	0.30±0.07

Table 4. Best-fit power laws to the whole cluster region over the mass range 0.2–0.6 $M_\odot$ for a 1 Myr isochrone and 0.3–0.7 $M_\odot$ for a 2 Myr isochrone.

Age Myr	Filters	Dist kpc	$log(\frac{Z}{Z_\odot})$	Γ
1	F162M,F182M	4.5	0	−1.0±0.54
2	F162M,F182M	4.5	0	−1.4±0.56
1	F162M,F200W	4.5	0	−1.3±0.73
2	F162M,F200W	4.5	0	−0.8±0.66
1	F162M,F182M	4.5	−0.5	−1.0±0.54
2	F162M,F182M	4.5	−0.5	−1.0±0.33
1	F162M,F200W	4.5	−0.5	−1.3±0.73
2	F162M,F200W	4.5	−0.5	−0.8±0.66

and $\sigma = 0.34$. Thus, the impact of using this different extinction law is very minor for the range of extinction values in this study.

The field IMF peaks at 0.25 $M_\odot$ for the system IMF. Thus, if the binary properties were different at low metallicity this could affect the comparison. However, even the single-object IMF in Chabrier (2005) only sees a shift in the peak mass to 0.2 $M_\odot$, marginally consistent with the highest peak masses that we determined. Furthermore, Machida et al. (2009) suggests from theory that the binary fraction should be higher in a low-metallicity star-forming region, which would only lower the deduced single object IMF from the fits in Table 2.

The IMFs and thus peak masses could be biased by the usage of the solar-metallicity isochrones. To test for this, we fit log-normal distributions to the stellar range up to the saturation limit using the subsolar metallicity isochrones. For a distance of 4.5 kpc, we determined a peak mass of 0.13 ± 0.09 $M_\odot$ for 1 Myr and 0.26$M_\odot$ for the 2 Myr isochrones. The peak is about 10% higher for the 2 Myr isochrone compared to the peak for solar metallicity, but the conclusion remains the same. The 1 Myr isochrone provides a peak value consistent with that of the solar metallicity fits, but with larger uncertainties, mainly due to the more limited mass range and the peak being close to the lower mass limit.

4.6. Comparison with other IMF determinations

The local Galactic field population has been found to have a mass function that peaks at 0.25 $M_\odot$ (Chabrier 2005). Previous studies of nearby regions with solar metallicity have found results consistent with this (e.g., Andersen et al. 2008, using a sample of clusters studied spectroscopically). However, some variations from region to region have been observed (e.g., Bastian et al. 2010). For example, Damian et al. (2021) used a photometric sample of nine regions with variable depth in terms of limiting magnitude to determine an average peak mass of 0.32 ± 0.02 $M_\odot$ with an observed range from 0.18–0.44 $M_\odot$. Overall, the peak of the IMF measured here is on the lower side of the values determined for solar-metallicity regions.

In contrast, recent studies of the low-mass IMF in Galactic metal-poor environments have suggested a lower peak mass. The Digel Cloud 2 has a lower metallicity than S284, i.e., −0.7 dex. This region was imaged by Yasui et al. (2024), who determined a peak mass $\log(m_0) = -1.5 \pm 0.5$ ($0.03^{+0.07}_{-0.03}$ $M_\odot$). Their result would thus suggest that the peak mass of the IMF decreases relatively rapidly with decreasing metallicity. However, it should be noted that the isochrones used are different than the ones used here and in, for example, Gennaro & Robberto (2020), and the effects of crowding and nebulosity were gauged purely by photometric errors and not completeness calculations. Similarly, Yasui et al. (2023) suggest for the Galactic metal-poor region Sh2-209 that the IMF has a break mass at 0.1 $M_\odot$, but with the precise value depending on the distance and age of the system. The equivalent power law fitting to the local Galactic field population finds a break mass of 0.5 $M_\odot$ (Kroupa et al. 2026).

Previous studies, in for example the SMC and LMC, have been limited to the higher-mass part of the IMF, where the power-law index was found to be similar to that of the Galactic field IMF (Andersen et al. 2009; Da Rio et al. 2012). However, the field IMF in the dwarf galaxy Coma Berenices has suggested a higher peak mass of the IMF, despite the low metallicity of the galaxy (Gennaro et al. 2018). Note that the completeness limit in these studies was estimated at 0.23 $M_\odot$, barely reaching the Chabrier IMF peak. As noted in Andersen et al. (2017), when only one side of the log-normal is fit, there is some degeneracy between the peak mass and the width of the fit.

Thus, in summary, a picture is emerging of a possible change in the low-mass IMF toward lower peak masses for low-metallicity environments. This trend is in qualitative agreement with the simulations of Chon et al. (2021), although their simulations did not include magnetic fields or feedback mechanisms, which can limit fragmentation. In contrast, models such as that of Guszejnov et al. (2022) are more difficult to reconcile with this observational result.

The widths of the best-fit distributions appear, in general, to be narrower than that of the field IMF. A similar effect has been observed in some solar-metallicity regions, such as Westerlund 1 (Andersen et al. 2017). However, in this case, the narrower IMF is measured down to 0.03 $M_\odot$, compared to 0.2 $M_\odot$ in Westerlund 1.

The advent of deep, high-spatial-resolution near-infrared imaging with JWST now allows us to probe much larger ranges of parameter space to quantify variations in the IMF as a function of the environment. With this ability to probe the IMF across the Galaxy deep into the brown dwarf regime, improved models are needed to compare with the observations, both in terms of brown dwarf and stellar evolutionary models and simulations including the relevant physics with sufficient dynamical range to cover the low-mass IMF in complex environments.

4.7. Cluster mass

We can estimate the total mass of the cluster based on the measured part of the IMF. We adopted the log-normal results derived from the extinction-limited sample and extrapolated to higher masses using a combined mass function consisting of the log-normal fit below 1 $M_{\odot}$ and a Salpeter power law mass function above this value. Guarcello et al. (2021) found for Dolidze 25 as a whole that the IMF above 1 $M_{\odot}$ was consistent with having a Salpeter index, similar to results found in other low-metallicity environments; for example, in the Magellanic clouds.

The completeness prevented us from reaching the lowest masses in the central region, and thus we had to extrapolate the mass function there. This was done based on the radial profile in Fig. 8, i.e., for stars over a mass of 0.2 $M_{\odot}$. We compared the derived IMF in two radial bins to probe if any mass segregation might be evident that could skew the mass determination. For the 1 Myr F162M-F182M sample at a distance of 4.5 kpc, we determined the IMF in the annuli 0.13–0.46 pc and 0.46–0.66 pc. The peak masses are found to be 0.19 ± 0.04 $M_{\odot}$, and 0.15 ± 0.05 $M_{\odot}$, respectively, supporting an assumption that there is no mass segregation in the cluster.

The IMF was determined for the extinction-limited samples as discussed above. However, to obtain a better estimate of the total mass, we used all objects with an extinction above the lower extinction limit of 4.5 A_V. The total mass observed between the lower and upper mass limit for the IMF determination was then scaled to the full IMF as described above. Finally, it was also scaled to include the mass within 0.13 pc using the radial profile fit. For an assumed ago of 1 Myr, the estimated total mass is 160 $M_{\odot}$. If a 2 Myr age is assumed, the total mass is estimated to be 330 $M_{\odot}$. This mass is substantially lower than the gas mass estimated in Cheng et al. (2025), showing the system is gas-dominated and confirming its youth.

5. Conclusions

We have presented JWST NIRCam F162M, F182M, and F200W imaging of the embedded cluster S284-EC1 that is forming in a low-metallicity environment in the outer Galaxy. Our main conclusions are as follows:

1. The NIRCam images are sensitive to young stars and brown dwarfs between 0.6 $M_{\odot}$ (the saturation limit) and 0.03 $M_{\odot}$ (assuming a fiducial 1 Myr age and for an extinction of A_V = 15). The data are at least 60% complete to this mass limit outside a radius of 0.13 pc from the cluster center;
2. Log-normal fits to the IMF of the YSO population defined from an extinction-limited sample find the peak mass to be m_0 = 0.16 ± 0.02 $M_{\odot}$ This indicates a potential dependence of IMF properties on metallicity, which is consistent with an observational trend found in the lower-metallicity region Digel 2 (Yasui et al. 2024);
3. The main caveat associated with our result for the IMF peak mass is the dependence of the result on the assumed age of the population. However, a value of 1 Myr appears to be the most reasonable, given the embedded and star-forming nature of S284-EC1;
4. The overall current stellar mass of S284-EC1 is about 160 $M_{\odot}$ within a radius of 0.65 pc. There is no evidence of mass segregation within the cluster in the low-mass YSO population, although at least one massive star, currently $m_* \sim$ 10 $M_{\odot}$, appears to be forming in the cluster center.

Acknowledgements. This work is based [in part] on observations made with the NASA/ESA/CSA James Webb Space Telescope. The data were obtained from the Mikulski Archive for Space Telescopes at the Space Telescope Science Institute, which is operated by the Association of Universities for Research in Astronomy, Inc., under NASA contract NAS 5-03127 for JWST. These observations are associated with program 2317. AB acknowledges support from the Chalmers Astrophysics and Space Sciences Summer research program (CASSUM). JCT acknowledges support from ERC Advanced Grant 788829 (MSTAR). RF acknowledges financial support from the Severo Ochoa grant CEX2021-001131-S MICIU/AEI/10.13039/501100011033 and PID2023-146295NB-I00.

References

Allard, F. 2014, Exploring the Formation and Evolution of Planetary Systems, 299, 271
Allard, F., Homeier, D., & Freytag, B. 2012, Philos. Trans. Roy. Soc. Lond. A, 370, 2765
Andersen, M., Meyer, M. R., Oppenheimer, B., et al. 2006, AJ, 132, 2296
Andersen, M., Meyer, M. R., Greissl, J., et al. 2008, ApJ, 683, L183
Andersen, M., Zinnecker, H., Moneti, A., et al. 2009, ApJ, 707, 1347
Andersen, M., Gennaro, M., Brandner, W., et al. 2017, A&A, 602, A22
Ashraf, M., Jose, J., Herczeg, G. J., et al. 2026, ApJ, 998, 116
Baraffe, I., Homeier, D., Allard, F., et al. 2015, A&A, 577, A42
Bastian, N., Covey, K. R., & Meyer, M. R. 2010, ARA&A, 48, 339
Bate, M. R. 2025, MNRAS, 537, 752
Bate, M. R., Bonnell, I. A., & Bromm, V. 2002, MNRAS, 332, L65
Bate, M. R. 2014, MNRAS, 442, 285
Cardelli, J. A., Clayton, G. C., & Mathis, J. S. 1989, ApJ, 345, 245
Chabrier, G. 2005, The Initial Mass Function 50 Years Later, 327, 41
Cheng, Y., Tan, J. C., Andersen, M., et al. 2025, ApJ, 990, 173
Chon, S., Omukai, K. & Schneider, R. 2021, MNRAS, 508, 4175
Cusano, F., Ripepi, V., Alcalá, J. M., et al. 2011, MNRAS, 410, 227
Daflon, S., & Cunha, K. 2004, ApJ, 617, 1115
Da Rio, N., Gouliermis, D. A., Rochau, B., et al. 2012, MNRAS, 422, 3356
Damian, B., Jose, J., Samal, M. R., et al. 2021, MNRAS, 504, 2557
De Furio, M., Meyer, M. R., Greene, T., et al. 2025, ApJ, 981, L34
Fitzpatrick, E. L. 1999, PASP, 111, 63
Gaia Collaboration (Vallenari, A., et al.) 2023, A&A, 674, A1
Gennaro, M., & Robberto, M. 2020, ApJ, 896, 80
Gennaro, M., Brandner, W., Stolte, A., et al. 2011, MNRAS, 412, 2469
Gennaro, M., Geha, M., Tchernyshyov, K., et al. 2018, ApJ, 863, 38
Guarcello, M. G., Biazzo, K., Drake, J. J., et al. 2021, A&A, 650, A157
Guszejnov, D., Grudić, M. Y., Offner, S. S. R., et al. 2022, MNRAS, 515, 4929
Hennebelle, P., & Grudić, M. Y. 2024, ARA&A, 62, 63
Jadhav, O. R., Dewangan, L. K., Verma, A., et al. 2025, ApJ, 980, 133
Kalari, V. M., & Vink, J. S. 2015, ApJ, 800, 113
Kalirai, J. S., Anderson, J., Dotter, A., et al. 2013, ApJ, 763, 110
Kalari, V. M., Salinas, R., Andersen, M., et al. 2025, ApJ, 980, L16
Koornneef, J. 1982, A&A, 107, 247
Kroupa, P., Gjergo, E., Jerabkova, T., et al. 2026, Encyclop. Astrophys., 2, 173
Lennon, D. J., Dufton, P. L., Fitzsimmons, A., et al. 1990, A&A, 240, 349
Lindegren, L., Klioner, S. A., Hernández, J., et al. 2021, A&A, 649, A2
Machida, M. N., Omukai, K., Matsumoto, T., et al. 2009, MNRAS, 399, 1255
Mužić, K., Scholz, A., Peña Ramírez, K., et al. 2019, ApJ, 881, 79
Myers, A. T., Krumholz, M. R., Klein, R. I., et al. 2011, ApJ, 735, 49
Negueruela, I., Simón-Díaz, S., Lorenzo, J., et al. 2015, A&A, 584, A77
Patra, S., Jose, J., & Evans, N. J. 2024, ApJ, 970, 88
Phillips, M. W., Tremblin, P., Baraffe, I., et al. 2020, A&A, 637, A38
Puga, E., Hony, S., Neiner, C., et al. 2009, A&A, 503, 107
Rieke, M. J., Robertson, B., Tacchella, S., et al. 2023, ApJS, 269, 16
Robin, A. C., Luri, X., Reylé, C., et al. 2012, A&A, 543, A100
Russeil, D., Adami, C., & Georgelin, Y. M. 2007, A&A, 470, 161
Schmalzl, M., Gouliermis, D. A., Dolphin, A. E., et al. 2008, ApJ, 681, 290
Schneider, F. R. N., Ramírez-Agudelo, O. H., Tramper, F., et al. 2018, A&A, 618, A73
Stetson, P. B. 1987, PASP, 99, 191
Strampelli, G. M., Robberto, M., Pueyo, L., et al. 2024, ApJ, 967, 52 doi:10.1051/0004-6361/202243940
Yasui, C., Kobayashi, N., Saito, M., et al. 2023, ApJ, 943, 137
Yasui, C., Izumi, N., Saito, M., et al. 2024, ApJ, 975, 152
Zeidler, P., Sabbi, E., Nota, A., et al. 2024, ApJ, 975, 18
Zinnkann, M., Wirth, H., & Kroupa, P. 2024, A&A, 684, A108